A Nonbalanced Staggered-Grid FDTD Scheme for the First-Order Elastic-Wave Extrapolation and Reverse-Time Migration

Wenquan Liang, Guoxin Chen, Yanfei Wang, Jingjie Cao, and Jinxin Chen

***Abstract*—In this study, an efficient and accurate staggered-grid finite-difference time-domain method to solve the two-dimensional (2-D) first-order stress–velocity elastic-wave equation is proposed. In the conventional implementation of the staggered-grid finite-difference (SGFD) method, the same SGFD operator is used to approximate the spatial derivatives. However, we propose a numerical method based on the mixed SGFD operators that are more efficient but similar in accuracy when compared with a uniform SGFD operator. We refer to the proposed method as the nonbalanced SGFD numerical scheme that combines the high-order SGFD operators with the second-order SGFD operators. The suitability of the proposed scheme is verified by dispersion analysis. Through SGFD modeling and reverse-time migration examples, we demonstrate that the proposed nonbalanced scheme offers a similar level of accuracy with a lower computational cost compared with the time-consuming conventional SGFD method.**

***Index Terms*—Elastic waves, finite-difference methods, geophysics computing, reverse-time migration (RTM).**

I. Introduction

WAVE propagation in elastic solids has practical applications in seismic exploration, seismology, material science, geotechnical engineering, and other areas of research. To numerically simulate elastic-wave propagation, various numerical methods have been developed; examples include finite-difference [1]–[7], finite-volume [8], [9], finite-element [10], [11], and spectral element [12], [13] methods. The spectral element method has geometric flexibility of finite-element method and the accuracy of the spectral method; therefore, it has been used widely for wave equation modeling [12]–[14]. The most common method is finite difference, where the spatial derivatives of the partial differential equations are approximated by a finite difference on an equally spaced grid. The strength of finite difference is its simple numerical representation.

In staggered-grid finite-difference (SGFD), material properties are distributed in a staggered fashion at grid points. The SGFD method inherits the properties of a generic finite-difference method (i.e., simplicity and efficiency) [4], [14]–[24].

To suppress the issue of numerical dispersion, the SGFD has been effectively employed and rigorously studied. The grid dispersion of the SGFD method is primarily controlled by the discretization parameters, i.e., time and space steps. However, decreasing the spacing (time or space) to achieve the high-order accuracy affects the efficiency of the scheme. As an alternative, coarse-grid methods were developed in the form of high-order finite-difference methods, where large space steps are used in combination with long finite-difference stencils providing a reasonable accuracy [1], [2], [6], [7]. This high-order finite-difference method is now the prevalent numerical scheme for obtaining high accuracy. For example, time–space domain high-order FD scheme is proposed to suppress the space and time grid dispersion error simultaneously [25]. Simulate annealing, binomial windows, and optimized methods are used to determine the FD coefficients [7], [26], [27]. The large stencils typically provide a higher accuracy and reduce the number of grid points per minimum wavelength. However, the implementation of the long stencils results in an increased computational cost, particularly memory requirements.

Reverse-time migration (RTM) uses the full wavefield for imaging and is, therefore, a high-precision imaging method [28]–[36]. The basic step is the cross correlation between the forward and backward extrapolation wave fields. Liu *et al.* [37] proposed frequency-domain RTM based on Green's function. Zhang *et al.* [38] use high-order FDTD RTM for subsurface imaging. Li *et al.* [39] proposed Q-compensated RTM. These methods improved RTM imaging efficiency or accuracy. Wave mode separation is an important part of elastic RTM [40]–[43]. Deep learning methods are applied to wave mode separation in recent years [44], [45].

Manuscript received March 31, 2022; revised May 16, 2022; accepted June 1, 2022. Date of publication June 7, 2022; date of current version June 21, 2022. This work was supported in part by the National Natural Science Foundation of China under Grant 41904100, Grant 41704120, and Grant 41974166, in part by Fujian Outstanding Research Talent Cultivation Project, under IGGCAS Grant 2019031, in part by CAS Innovation Program under Grant ZDBS-LY-DQC003, and in part by the Open Research Fund of Key Laboratory of Engineering Geophysical Prospecting and Detection of Chinese Geophysical Society under Grant CJ2021GB01. *(Corresponding author: Guoxin Chen.)*

Wenquan Liang is with the School of Resource Engineering, Longyan University, Longyan 364000, China (e-mail: onethink2002@foxmail.com).

Guoxin Chen is with the Institute of Marine Geology and Resources, Ocean College, Zhejiang University, Zhoushan 316021, China, and also with the Key Laboratory of Engineering Geophysical Prospecting and Detection of Chinese Geophysical Society, Changjiang Geophysical Exploration and Testing Company Limited, Wuhan 430000, China (e-mail: zjucgx@zju.edu.cn).

Yanfei Wang is with the Key Laboratory of Petroleum Resources Research, Institute of Geology and Geophysics, Chinese Academy of Sciences, Beijing 100029, China (e-mail: yfwang@mail.iggcas.ac.cn).

Jingjie Cao is with the Hebei GEO University, Shijiazhuang 050031, China (e-mail: 472192892@qq.com).

Jinxin Chen is with the Institute of Marine Geology and Resources, Ocean College, Zhejiang University, Zhoushan 316021, China (e-mail: jinxinc@zju.edu.cn).

Digital Object Identifier 10.1109/JSTARS.2022.3181000

In this study, we propose a numerical method that reduces the cost of the coarse-grid methods using the large stencils by using two different finite-difference operators (long and short) of different sizes to compute the spatial derivatives. Both the long and short stencils are used simultaneously to evaluate the spatial derivatives within a time step. A careful approach is considered when computing the SGFD coefficients for the long stencil, which cancels out the error produced by the short operators. We refer to this as a nonbalanced SGFD scheme.

The approach of using finite-difference operators of different sizes in a single simulation has already been proposed [46], but in this study, we uniquely combine a large finite-difference stencil with a short second-order finite-difference operator. A similar method has already been successfully applied to solve the acoustic wave equation [47]. In this study, we illustrate the efficiency of this method by applying it to the elastic-wave equation, which has mixed spatial derivatives. The proposed method achieves accuracy similar to that of the coarse-grid and long stencil methods but with 40% less computational cost.

The rest of this paper is organized as follows. In Section II, we rigorously define the nonbalanced SGFD method. In Section III, we define the method to compute the finite-difference coefficients using the dispersion relation of the implementation. Then, in Section IV, we analyze the stability of the proposed numerical scheme. In Sections V and VI, we perform computational experiments and RTM of different elastic models and show the efficiency of the proposed nonbalanced SGFD scheme. Finally, some concluding remarks are given.

II. Nonbalanced SGFD Scheme

The time-domain equations for wave propagation in a heterogeneous elastic medium can be found in Virieux [4]. The two-dimensional (2-D) velocity–stress equation for elastic-wave propagation in the (x, z) plane is expressed as follows:

$$\begin{cases} \frac{\partial \tau_{xx}}{\partial t} = (\lambda + 2\mu)\frac{\partial v_x}{\partial x} + \lambda \frac{\partial v_z}{\partial z} \\ \frac{\partial \tau_{zz}}{\partial t} = (\lambda + 2\mu)\frac{\partial v_z}{\partial z} + \lambda \frac{\partial v_x}{\partial x} \\ \frac{\partial \tau_{xz}}{\partial t} = \mu\left(\frac{\partial v_z}{\partial x} + \frac{\partial v_x}{\partial z}\right) \\ \rho \frac{\partial v_x}{\partial t} = \frac{\partial \tau_{xx}}{\partial x} + \frac{\partial \tau_{xz}}{\partial z} \\ \rho \frac{\partial v_z}{\partial t} = \frac{\partial \tau_{zz}}{\partial z} + \frac{\partial \tau_{xz}}{\partial x} \end{cases} \tag{1}$$

where $(\tau_{xx}, \tau_{zz}, \tau_{xz})$ represents the stress components, (v_x, v_z) is the velocity vector, λ and μ are the Lame coefficients, and ρ is the density of the medium. To solve the system of the elastic wave (1) numerically, the spatial derivatives in (1) is usually approximated with the same SGFD operator. We referred to this SGFD scheme as the conventional SGFD scheme. We introduced different SGFD operators, referred to as the nonbalanced SGFD scheme, for different spatial derivatives in (1), as in the following (2) shown at the bottom of this page.

where $u_{i,j}^{[k}] = u(x + ih, z + jh, t + k\Delta t)$, $u = [v_x, v_z, \tau_{xx}, \tau_{zz}, \tau_{xz},]$, M ($M = 7$) is the SGFD operator length, c_m (for each m) is the SGFD operator coefficient, Δt is the temporal grid interval, and h is the distance between the two consecutive space grid points.

Let us take a closer look at (1) and its discretized scheme equation (2). There are eight different spatial derivatives in (1). For (2), each has four SGFD operators with $M = 7$ and four SGFD operators with $M = 1$.

The key component in the proposed nonbalanced SGFD scheme is the usage of the short SGFD operator for half of the spatial derivatives in (2). The numerical schemes in (2) are defined as the *nonbalanced SGFD scheme* as they are not balanced for its SGFD operator length.

At first, the nonbalanced SGFD scheme (2) may not seem as attractive as some spatial derivatives are approximated with the second-order SGFD operators that would result in spatial grid dispersion. However, specially designed SGFD coefficients for the nonbalanced SGFD scheme can result in reduced grid dispersion and improved numerical simulation efficiency.

III. Coefficients of the Nonbalanced SGFD Scheme

Substitution of the first three equations of (1) into the last two equations of (1) yields the second-order elastic-wave equation. The matrix form of the second-order elastic-wave equation in the frequency wavenumber domain is expressed as follows [5]:

$$\begin{pmatrix} -\alpha^2 k_x^2 - \beta^2 k_z^2 - D'_{tt} & -\left(\alpha^2 - \beta^2\right) k_x k_z \\ -\left(\alpha^2 - \beta^2\right) k_x k_z & -\alpha^2 k_z^2 - \beta^2 k_x^2 - D'_{tt} \end{pmatrix} \begin{pmatrix} v'_x \\ v'_z \end{pmatrix} = 0 \tag{3}$$

where D'_{tt} is the finite-difference operator of the second-order time derivative in the frequency wavenumber domain, k_x and k_z are the spatial wavenumbers in the x and z directions, respectively, v'_x and v'_z are the frequency wavenumber domains v_x and v_z, respectively, and β and α are the *S*- and *P*-wave velocities, respectively:

$$\alpha^2 = (\lambda + 2\mu)/\rho \tag{4}$$

$$\beta^2 = \mu/\rho. \tag{5}$$

$$\begin{cases} \frac{\tau_{xx}\left[\begin{smallmatrix}1/2\\1/2,0\end{smallmatrix}\right] - \tau_{xx}\left[\begin{smallmatrix}-1/2\\1/2,0\end{smallmatrix}\right]}{\Delta t} = \frac{(\lambda+2\mu)}{h}\left[v_x\left[\begin{smallmatrix}0\\1,0\end{smallmatrix}\right] - v_x\left[\begin{smallmatrix}0\\0,0\end{smallmatrix}\right]\right] + \frac{\lambda}{h}\left[v_z\left[\begin{smallmatrix}0\\1/2,1/2\end{smallmatrix}\right] - v_z\left[\begin{smallmatrix}0\\1/2,-1/2\end{smallmatrix}\right]\right] \\ \frac{\tau_{zz}\left[\begin{smallmatrix}1/2\\1/2,0\end{smallmatrix}\right] - \tau_{zz}\left[\begin{smallmatrix}-1/2\\1/2,0\end{smallmatrix}\right]}{\Delta t} = \frac{\lambda}{h}\left[v_x\left[\begin{smallmatrix}0\\1,0\end{smallmatrix}\right] - v_x\left[\begin{smallmatrix}0\\0,0\end{smallmatrix}\right]\right] + \frac{(\lambda+2\mu)}{h}\left[v_z\left[\begin{smallmatrix}0\\1/2,1/2\end{smallmatrix}\right] - v_z\left[\begin{smallmatrix}0\\1/2,-1/2\end{smallmatrix}\right]\right] \\ \frac{\tau_{xz}\left[\begin{smallmatrix}1/2\\0,1/2\end{smallmatrix}\right] - \tau_{xz}\left[\begin{smallmatrix}-1/2\\0,1/2\end{smallmatrix}\right]}{\Delta t} = \frac{\mu}{h}\sum_{m=1}^{M} c_m\left[v_z\left[\begin{smallmatrix}0\\m-1/2,1/2\end{smallmatrix}\right] - v_z\left[\begin{smallmatrix}0\\-m+1/2,1/2\end{smallmatrix}\right] + v_x\left[\begin{smallmatrix}0\\0,m\end{smallmatrix}\right] - v_x\left[\begin{smallmatrix}0\\0,-m+1\end{smallmatrix}\right]\right] \\ \frac{v_x\left[\begin{smallmatrix}1\\0,0\end{smallmatrix}\right] - v_x\left[\begin{smallmatrix}0\\0,0\end{smallmatrix}\right]}{\Delta t} = \frac{1}{\rho}\left\{\frac{1}{h}\sum_{m=1}^{M} c_m\left[\tau_{xx}\left[\begin{smallmatrix}1/2\\m-1/2,0\end{smallmatrix}\right] - \tau_{xx}\left[\begin{smallmatrix}1/2\\-m+1/2,0\end{smallmatrix}\right]\right] + \frac{1}{h}\left[\tau_{xz}\left[\begin{smallmatrix}1/2\\0,1/2\end{smallmatrix}\right] - \tau_{xz}\left[\begin{smallmatrix}1/2\\0,-1/2\end{smallmatrix}\right]\right]\right\} \\ \frac{v_z\left[\begin{smallmatrix}1\\1/2,1/2\end{smallmatrix}\right] - v_z\left[\begin{smallmatrix}0\\1/2,1/2\end{smallmatrix}\right]}{\Delta t} = \frac{1}{\rho}\left\{\frac{1}{h}\left[\tau_{xz}\left[\begin{smallmatrix}1/2\\1,1/2\end{smallmatrix}\right] - \tau_{xz}\left[\begin{smallmatrix}1/2\\0,1/2\end{smallmatrix}\right]\right] + \frac{1}{h}\sum_{m=1}^{M} c_m\left[\tau_{zz}\left[\begin{smallmatrix}1/2\\1/2,m\end{smallmatrix}\right] - \tau_{zz}\left[\begin{smallmatrix}1/2\\1/2,-m+1\end{smallmatrix}\right]\right]\right\} \end{cases} \tag{2}$$

The two roots of (3) yield the following dispersion relation:

$$\alpha^2 k_x^2 + \alpha^2 k_z^2 - D'_{tt} = 0 \tag{6}$$

$$\beta^2 k_x^2 + \beta^2 k_z^2 - D'_{tt} = 0. \tag{7}$$

Either (6) or (7) could be used to determine the SGFD operator coefficients. Because the velocity value of β is smaller than α, (7) is usually utilized to determine the SGFD operator coefficient as small velocity has larger numerical dispersion errors.

For the conventional SGFD scheme, the spatial derivative can be approximated by the following SGFD operator:

$$\frac{\partial u}{\partial x} = \frac{1}{h}\sum_{m=1}^{M} c_m \left(u_{m-1/2} - u_{-m+1/2}\right). \tag{8}$$

By applying the Fourier transform to the SGFD operator in (8), we one can obtain

$$k = \frac{1}{h}\sum_{m=1}^{M} c_m \left(\sin\left[(m-0.5)kh\right]\right). \tag{9}$$

Then, the following frequency wavenumber dispersion relation can be obtained from (7) for the conventional SGFD scheme [47]

$$\left[\sum_{m=1}^{M} c_m \sin((m-0.5)k_x h)\right]^2 + \left[\sum_{m=1}^{M} c_m \sin((m-0.5)k_z h)\right]^2 = \frac{1-\cos(k\beta\Delta t)}{2r^2} \tag{10}$$

where $r = \beta\Delta t/h$ and $(k_x, k_z) = k(\cos\theta, \sin\theta)$, in which θ is the plane wave-propagation angle measured from the horizontal plane perpendicular to the z-axis. Equation (10) can be used to calculate the SGFD coefficients in the time–space domain for the conventional SGFD scheme, as shown in [48].

For the nonbalanced SGFD scheme, the following equation can be obtained similarly from (7):

$$2\sin\frac{k_z h}{2}\sum_{m=1}^{M} c_m \left(\sin(m-0.5)k_z h\right) + 2\sin\frac{k_x h}{2}\sum_{m=1}^{M} c_m \left(\sin(m-0.5)k_x h\right) = \frac{1-\cos(k\beta\Delta t)}{2r^2} \tag{11}$$

where the unknowns are the SGFD operator coefficients c_m for all m. Equation (11) can be used to calculate the SGFD coefficients in the time–space domain for the nonbalanced SGFD scheme, as shown in [47]. It should be noted that when we determine the SGFD coefficients in the time–space domain using (11), the SGFD coefficient is related to the wave-propagation velocity β.

IV. Dispersion and Stability Analyses

Here, we compare the numerical errors in solutions obtained from the conventional and nonbalanced SGFD schemes in the time–space domain. The numerical error δ of the conventional SGFD scheme for the *P*-wave is described by Liu and Sen [49] as follows:

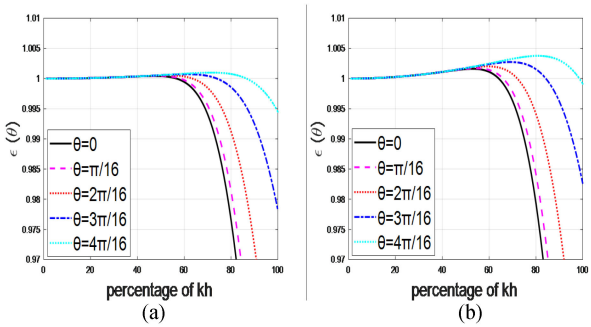

Fig. 1. Numerical error curves of the conventional SGFD scheme with the nonoptimized operator coefficients for 2-D elastic-wave equation with $\alpha = 2598$ m/s, $\beta = 1500$ m/s, $h = 20$ m, $M = 7$, and $\tau = 1$ ms. (a) *S*-wave. (b) *P*-wave.

$$\delta(\theta) = \frac{\alpha_{FD}}{\alpha} = \frac{2}{rkh}\sin^{-1}\left(r\sqrt{q_1}\right) \tag{12}$$

where

$$q_1 = \left(\sum_{m=1}^{M} c_m \sin\left[(m-0.5)\,kh\cos\theta\right]\right)^2 + \left(\sum_{m=1}^{M} c_m \sin\left[(m-0.5)\,kh\sin\theta\right]\right)^2. \tag{13}$$

Similarly, the numerical error δ of the conventional SGFD scheme for the *S*-wave could also be obtained. The numerical error δ of the nonbalanced SGFD scheme for the *P*-wave is defined by

$$\delta(\theta) = \frac{\alpha_{FD}}{\alpha} = \frac{2}{rkh}\sin^{-1}\left(r\sqrt{q_2}\right) \tag{14}$$

where

$$q_2 = \sin\left(0.5kh\cos\theta\right)\sum_{m=1}^{M} c_m \sin\left[(m-0.5)\,kh\cos\theta\right] + \sin\left(0.5kh\sin\theta\right)\sum_{m=1}^{M} c_m \sin\left[(m-0.5)\,kh\sin\theta\right]. \tag{15}$$

Similar to (14), the numerical error δ of the nonbalanced SGFD scheme for the *S*-wave could also be obtained.

Figs. 1–3 illustrate the numerical error for the different SGFD schemes for a homogeneous 2-D elastic model. Results in Fig. 1 are obtained by using the conventional SGFD scheme with coefficients calculated by the Taylor expansion. The absolute value of the numerical error is < 0.005 (within 70% of the *kh* range). Fig. 2 represents the error plots for the conventional SGFD scheme with coefficients calculated by the least squares method (referred to here as the *optimized solution*). When considering an error < 0.005 obtained from the Taylor expansion, we note that the optimized SGFD operator coefficients can suppress the numerical error in a larger wavenumber range (see Fig. 2) than

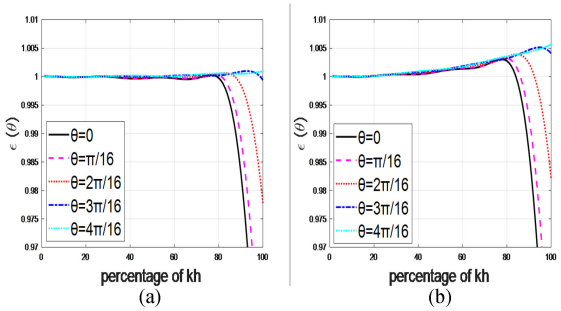

Fig. 2. Numerical error curves of the conventional SGFD scheme with the optimized operator coefficient for 2-D elastic-wave equation with $\alpha = 2598$ m/s, $\beta = 1500$ m/s, $h = 20$ m, $M = 7$, and $\tau = 1$ ms. (a) *S*-wave. (b) *P*-wave.

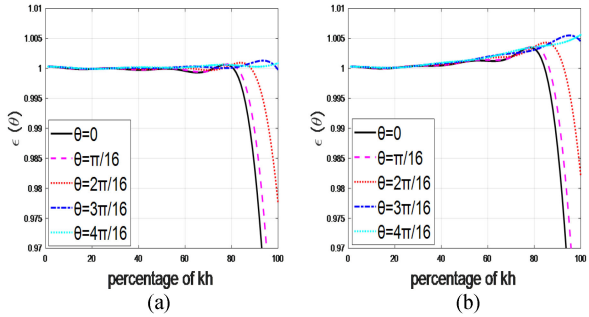

Fig. 3. Numerical error curves of the nonbalanced SGFD scheme with the optimized operator coefficient for 2-D elastic-wave equation with $\alpha = 2598$ m/s, $\beta = 1500$ m/s, $h = 20$ m, $M = 7$, and $\tau = 1$ ms. (a) *S*-wave. (b) *P*-wave.

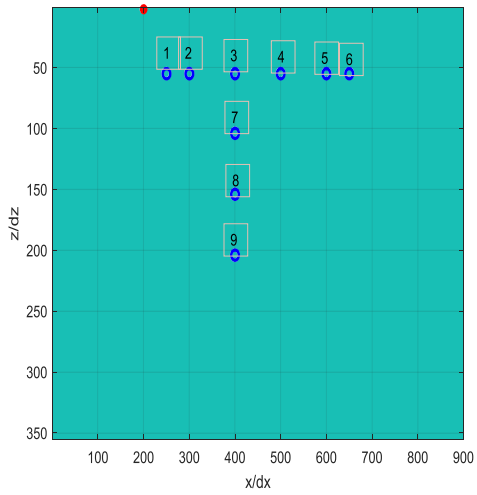

Fig. 4. Source (red circle) and receiver (blue circles numbered 1–9) locations.

the nonoptimized SGFD (see Fig. 1). The results of Fig. 3 were obtained using the proposed nonbalanced SGFD scheme with coefficients calculated by the least squares method. From Figs. 2 and 3, we conclude that the precision of the proposed nonbalanced SGFD scheme is similar to the conventional scheme.

The commonly used nonbalanced first-order SGFD coefficients computed in the space domain for (2) are shown in Table I [obtained by the least squares solution of (9)]. These coefficients are also used for the computational experiment presented in this article.

TABLE I
OPTIMIZED FIRST-ORDER SGFD COEFFICIENTS FOR THE NONBALANCED FD SCHEME

	C_1	C_2	C_3	C_4	C_5	C_6	C_7
M=3	1.40887	−0.16472	0.01727 1				
M=5	1.53147	−0.252544	0.06074 7	−0.0135055	0.001991 32		
M=7	1.59906	−0.310692	0.10345	−0.0398274	0.015085 7	−0.00487 87	0.001042

From (6) and (7), we can obtain the following equations for the conventional SGFD scheme [5]:

$$\sin^2(0.5\omega\tau) = \left(\frac{\Delta t\beta}{h}\right)^2 \left(X^2 + Z^2\right) \tag{16}$$

$$\sin^2(0.5\omega\tau) = \left(\frac{\Delta t\alpha}{h}\right)^2 \left(X^2 + Z^2\right) \tag{17}$$

where

$$X = \sum_{m=1}^{M} c_m \sin\left((m - 0.5)\, k_x h\right) \tag{18}$$

$$Z = \sum_{m=1}^{M} c_m \sin\left((m - 0.5)\, k_z h\right). \tag{19}$$

If both types of waves (*P* and *S*) are generated and propagated in a medium, the condition in (17) for the *P*-wave has to be considered as the joint stability condition, as α is large. Once the stability condition for α is satisfied, then the condition naturally extends for β.

From (17), we obtain

$$\left(\frac{\Delta t\alpha}{h}\right)^2 \left(X^2 + Z^2\right) \le 1. \tag{20}$$

Equation (20) gives a stability condition for the conventional SGFD scheme (with $k_x h = \pi$, $k_z h = \pi$)

$$\left(\frac{\Delta t\alpha}{h}\right) \le 1/\sqrt{\left(X^2 + Z^2\right)} \le \frac{1}{\sqrt{2}\sum_{m=1}^{M} |c_m|}. \tag{21}$$

For the proposed nonbalanced SGFD scheme

$$X'^2 = \sin(0.5k_x h) \sum_{m=1}^{M} c_m \left(\sin\left((m - 0.5)\, k_x h\right)\right) \tag{22}$$

$$Z'^2 = \sin(0.5k_z h) \sum_{m=1}^{M} c_m \left(\sin\left((m - 0.5)\, k_z h\right)\right). \tag{23}$$

Similarly, the stability condition for the proposed nonbalanced SGFD scheme is expressed as

$$r = \left(\frac{\Delta t\alpha}{h}\right) \le 1/\sqrt{\left(X'^2 + Z'^2\right)} \le s = \frac{1}{\sqrt{2\sum_{m=1}^{M} |c_m|}}. \tag{24}$$

Next, we demonstrate the effectiveness of the stability condition in (24) with an example. We use the SGFD coefficients

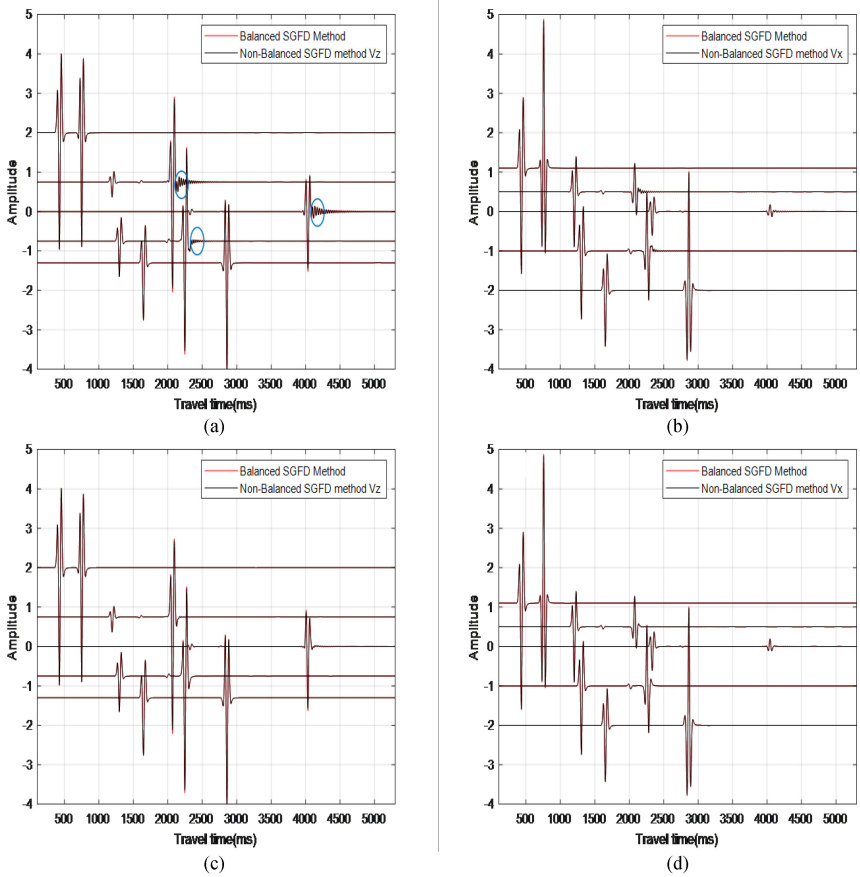

Fig. 5. Comparison of seismograms obtained at receivers 1, 3, 5, 7, and 9 from the top to the bottom. (a) v_z component obtained with the conventional and the nonbalanced SGFD scheme with $M = 4$. (b) v_x component obtained with the conventional and the nonbalanced SGFD scheme with $M = 4$. (c) v_z component obtained with the conventional and the nonbalanced SGFD scheme with $M = 7$. (d) v_x component obtained with the conventional and the nonbalanced SGFD scheme with $M = 7$.

for $M = 7$ in Table I. The stability condition is calculated as $r \leq 1/\left(\sqrt{2\sum_{m=1}^{M}|c_m|}\right) = 0.491$. Let $h = 10$ m and $\Delta t = 0.001$ s. Therefore, from (24), if $\alpha = 4912$ m/s, it should be unstable. However, if $\alpha = 4908$ m/s, the scheme will be stable. We used numerical simulation to verify this stability condition with a homogeneous model. Our calculations show that if $\alpha = 4912$ m/s, $h = 10$ m, and $\Delta t = 0.001$ s, the numerical process is unstable, whereas for $\alpha = 4908$ m/s, $h = 10$ m, and $\Delta t = 0.001$ s, it is stable.

V. Numerical Simulations

To validate the numerical scheme, we compared the numerical solution obtained for a homogeneous model. The discretization parameters for the SGFD operator are $dx = dz = 10$ m, $\Delta t =$ 1 ms, $M = 7$, $\alpha = 1732.1$ m/s, and $\beta = 1000$ m/s. We consider a seismic source and receiver locations, as shown in Fig. 4. A Ricker wavelet with a central frequency at 14 Hz is used as the seismic source.

The time history of particle velocities v_z and v_x is computed at five different receiver locations using the conventional and the nonbalanced SGFD scheme (see Fig. 5). Fig. 5(a) and (b) shows that the seismograms are almost identical for the conventional and the nonbalanced SGFD schemes with $M = 4$. There is a space grid dispersion on both [blue eclipse in Fig. 5(a) and (b)]. Similarly, Fig. 5(c) and (d) shows that the seismograms are almost identical for the conventional and nonbalanced SGFD scheme with $M = 7$. The space grid dispersion is suppressed with the increase in the SGFD operator length [blue eclipse in Fig. 5(c) and (d)]. Fig. 5(a)–(d) shows the seismograms almost identical for the conventional and nonbalanced SGFD schemes.

Next, we consider the salt velocity model (see Fig. 6). In this example, we used the long SGFD operator as the analytical method ($M = 30$).

Fig. 7(a) and (b) represents the seismic record of the v_z component computed using the conventional SGFD scheme (with nonoptimized SGFD coefficient) and the nonbalanced SGFD scheme (with optimized $M = 7$ SGFD coefficients in Table I), respectively. Fig. 7(c) shows the seismic record of the v_z component obtained by the conventional SGFD scheme with $M = 30$ (with nonoptimized SGFD coefficient). In Fig. 7(d), seismograms are extracted from Fig. 7(a)–(c). From Fig. 7(d) and (e), we observed that the results of the nonbalanced SGFD scheme are very close to the conventional SGFD scheme with a very long SGFD operator ($M = 30$).

Fig. 8(a) and (b) represents the seismic record of the τ_{xx} component computed with the conventional SGFD and the

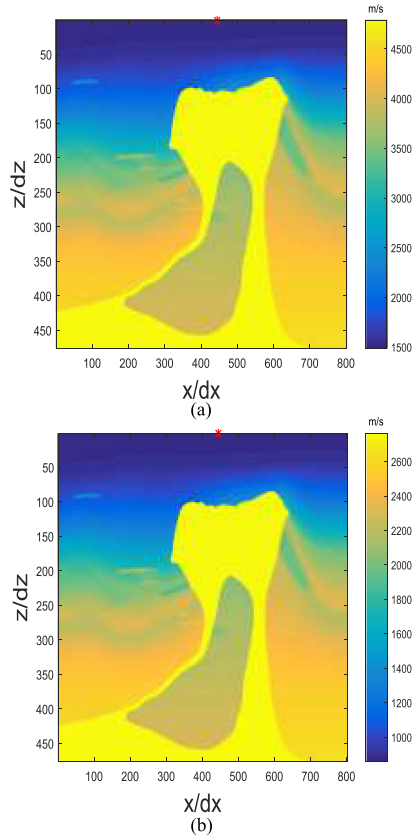

Fig. 6. Salt velocity model. (a) *P*-wave velocity model. (b) *S*-wave velocity model.

nonbalanced SGFD scheme, respectively. Fig. 8(c) shows the seismic record of the τ_{xx} component obtained by the conventional SGFD scheme with $M = 30$. Fig. 8(d) shows seismograms slices extracted from Fig. 8(a)–(c). Fig. 8(d) and (e) demonstrates that the results obtained from the nonbalanced SGFD scheme and the conventional SGFD scheme with a very long SGFD operator ($M = 30$) are in excellent agreement.

In theory, assuming that the simulation time for the traditional conventional SGFD scheme is $M + M$, then the simulation time for the nonbalanced SGFD scheme should be $M + 1$. It took 962 s to achieve the simulated wave field, as shown in Fig. 8(a), but only 553 s to achieve the simulated wave field, as shown in Fig. 8(b). This agrees with the analysis as 553/962 is approximately equal to $(M + 1)/(M + M)$, where $M = 7$ (i.e., 8/14). Therefore, the nonbalanced SGFD scheme can save approximately 42% of the simulation time compared with the conventional SGFD scheme.

VI. Reverse-Time Migration

To further verify the performance of the nonbalanced SGFD, we apply it to the RTM of elastic waves. Unlike the RTM based on scalar acoustic waves, only the *P*-wave field needs to be considered, while the RTM based on elastic waves needs to consider the coupling problem of the *P*- and *S*-wave and the converted wave fields. Thus, doing wave mode decomposition before performing ERTM is necessary. Based on the comprehensive consideration of the decomposition effect and computational efficiency, mode decomposition based on the first-order velocity stress elastic-wave equation to separate the *P*- and *S*-wave is applied [32], [34]. Combining (1) and (25), pure *P*-wave source wave field $U^p(x,t)$ and pure *S*-wave source wave field $U^s(x,t)$ can be obtained

$$\begin{cases} \frac{\partial \tau_{xx}^p}{\partial t} = (\lambda + 2\mu)\left(\frac{\partial v_x}{\partial x} + \frac{\partial v_z}{\partial z}\right) \\ \frac{\partial \tau_{zz}^p}{\partial t} = (\lambda + 2\mu)\left(\frac{\partial v_x}{\partial x} + \frac{\partial v_z}{\partial z}\right) \\ \frac{\partial v_z^p}{\partial t} = \frac{1}{\rho}\frac{\partial \tau_{zz}^p}{\partial z} \\ \frac{\partial v_x^p}{\partial t} = \frac{1}{\rho}\frac{\partial \tau_{xx}^p}{\partial x} \\ v_x^s = v_x - v_x^p \\ v_z^s = v_z - v_z^p \end{cases} \tag{25}$$

where τ_{xx}^p and τ_{zz}^p are the stress components of the *p*-wave, and v_x^p and v_z^p are the horizontal and vertical velocity components of the *P*-wave, respectively. v_x^s and v_z^s are the horizontal and vertical velocity components of the *S*-wave, respectively.

After obtaining the source wave field, the next step is to obtain the corresponding backpropagation wave field. The backpropagation *P*-wave wave field $R^p(x,t)$ and the backpropagation *S*-wave wave field $R^s(x,t)$ are obtained from the following:

$$\begin{cases} \frac{\partial \tau_{xx}}{\partial t} = (\lambda + 2\mu)\frac{\partial v_x}{\partial x} + \lambda\frac{\partial v_z}{\partial z} \\ \frac{\partial \tau_{zz}}{\partial t} = (\lambda + 2\mu)\frac{\partial v_z}{\partial z} + \lambda\frac{\partial v_x}{\partial x} \\ \frac{\partial \tau_{xz}}{\partial t} = \mu\left(\frac{\partial v_z}{\partial x} + \frac{\partial v_x}{\partial z}\right) \\ \rho\frac{\partial v_x}{\partial t} = \frac{\partial \tau_{xx}}{\partial x} + \frac{\partial \tau_{xz}}{\partial z} \\ \rho\frac{\partial v_z}{\partial t} = \frac{\partial \tau_{zz}}{\partial z} + \frac{\partial \tau_{xz}}{\partial x} \\ v_x(x_R, z_R, t) = u_x^{obs}(x_R, z_R, t)| \\ v_z(x_R, z_R, t) = u_z^{obs}(x_R, z_R, t) \\ 0 \le t \le T \end{cases} \tag{26}$$

where $u_x^{obs}(x_R, z_R, t)$ and $u_z^{obs}(x_R, z_R, t)$ are the horizontal and vertical component of the seismic record, respectively, x_R and z_R are the receiver positions, and T is the maximum of the seismic record time. Equations (25) and (26) are discretized by using the nonbalanced SGFD scheme similar to (2).

To solve the polarity reversal problem, the vector imaging condition is utilized [32]–[34]

$$I_{mn}(x,z) = \frac{\sum_{SRT} U^m(x,z,t) \cdot R^n(x,z,t)}{\sum_{SRT} U^m(x,z,t) \cdot U^n(x,z,t)} \tag{27}$$

where $\cdot$ means the inner product, $m = \{p,s\}, n = \{p,s\}$ and $I_{mn}(x,z)$ means image from different kinds of wave fields.

The chosen velocity model simulates marine seismic exploration; the received seismic data are mainly the *P*-wave data and the *S*-wave data, which are converted from the *P*-wave. Therefore, we adopt $I_{PP}(x,z)$ and $I_{PS}(x,z)$ as the image result of the *P*- and *S*-wave, respectively. Fig. 9 shows the parameters of the Marmousi model. Figs. 10 and 11 show the imaging results. From Figs. 10 and 11, it can be observed that the proposed nonbalanced SGFD scheme can be used for first-order elastic RTM of complex velocity model with a similar accuracy as the conventional one. But in terms of computational time, the nonbalanced SGFD scheme only uses 60.9% of the conventional method.

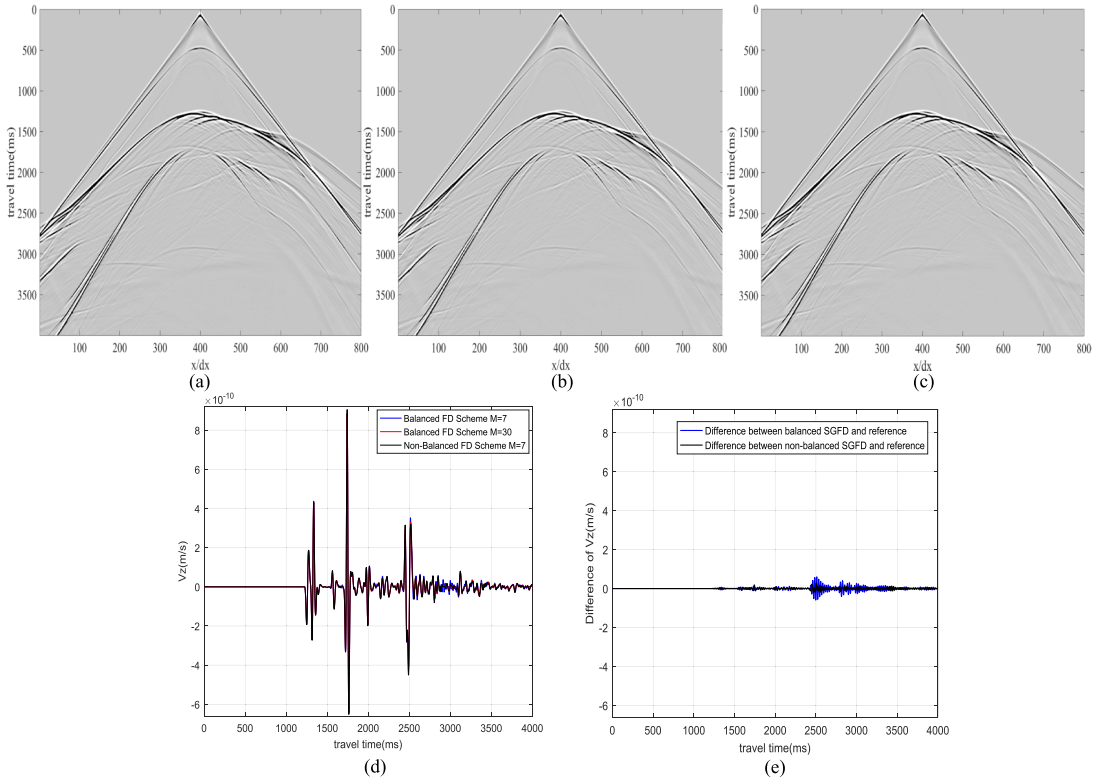

Fig. 7. Seismic records of the v_z component. (a) Conventional SGFD scheme ($M = 7$). (b) Nonbalanced SGFD scheme ($M = 7$). (c) Conventional SGFD scheme ($M = 30$). (d) Slices of seismograms extracted from (a) to (c) at $x/dx = 222$. (e) Difference in seismograms from (d).

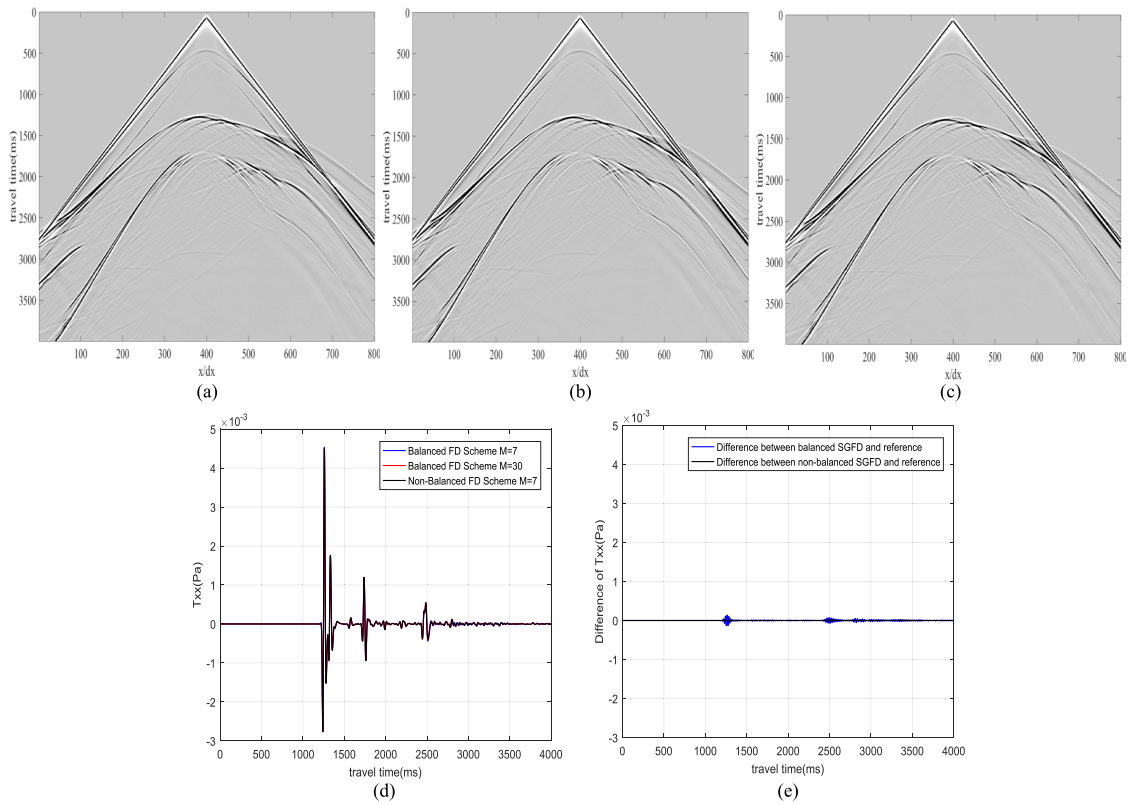

Fig. 8. Seismic records of τ_{xx} component. (a) Conventional SGFD scheme. (b) Nonbalanced SGFD scheme. (c) Conventional SGFD scheme ($M = 30$). (d) Slices of seismograms extracted from (a) to (c) at $x/dx = 222$. (e) Difference in seismograms from (d).

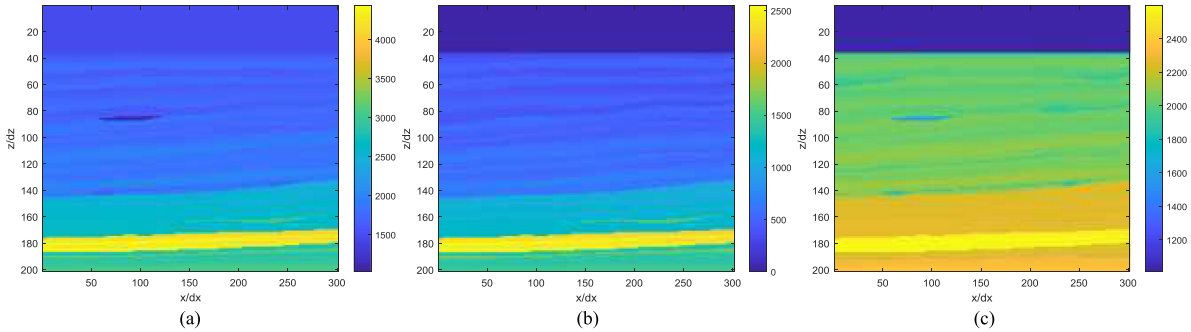

Fig. 9. Marmousi model. (a) *P*-wave velocity model. (b) *S*-wave velocity model. (c) Density model.

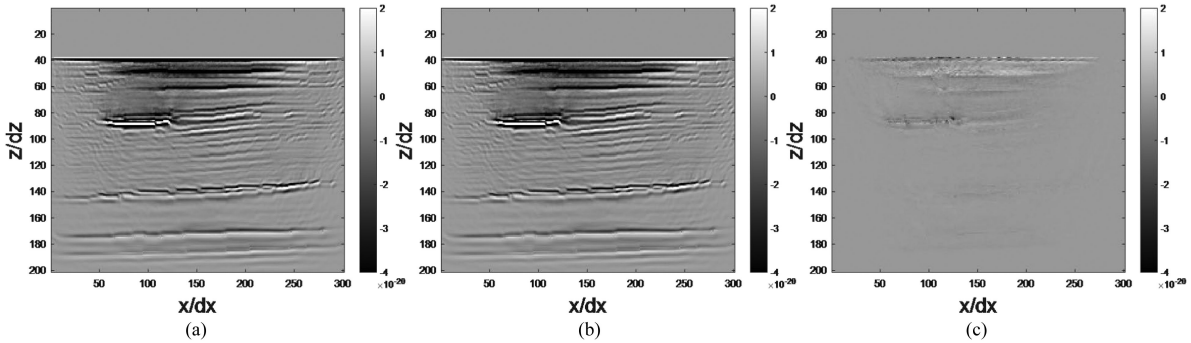

Fig. 10. Migration image $I_{PP}(x, z)$. (a) With the conventional SGFD scheme. (b) With the proposed SGFD scheme. (c) 10×(the difference).

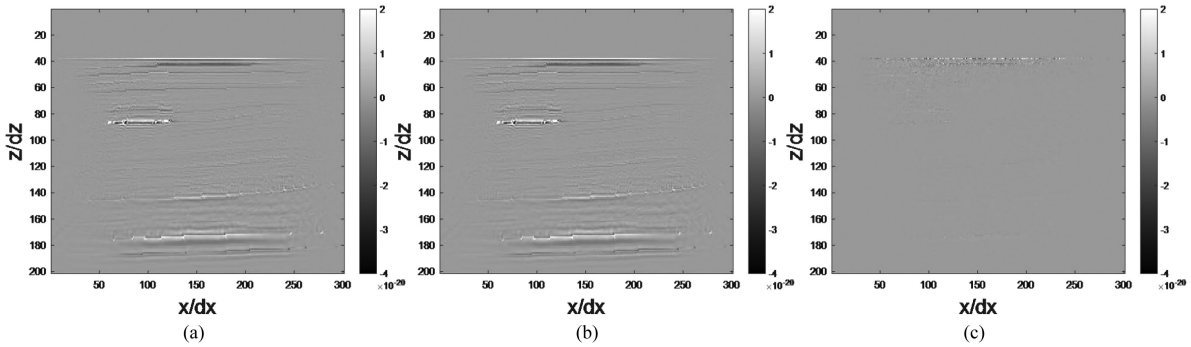

Fig. 11. Migration image $I_{PS}(x, z)$. (a) With the conventional SGFD scheme. (b) With the proposed SGFD scheme. (c) 10×(the difference).

VII. Conclusion

In this study, we proposed a nonbalanced SGFD scheme for solving the 2-D elastic-wave equation and RTM. We give the SGFD operator coefficients for the proposed nonbalanced SGFD scheme in Table I. The numerical solution error obtained from the nonbalanced SGFD scheme was similar when compared with the conventional SGFD operator. Computational experiments were performed to illustrate the advantages of the proposed SGFD scheme. The proposed numerical scheme was also carried out for a salt velocity model with results compared against the existing implementation of SGFD schemes. The results show that, with the nonbalanced SGFD scheme and the corresponding finite-difference operator coefficients, less computational time is required to compute the numerical simulation without losing accuracy. The migration image of the Marmousi model is also very similar. Therefore, we conclude that the nonbalanced SGFD can be considered as a useful tool for the elastic-wave extrapolation and RTM.

References

[1] R. M. Alford, K. R. Kelly, and D. M. Boore, "Accuracy of finite-difference modeling of the acoustic wave equation," *Geophysics*, vol. 39, no. 6, pp. 834–842, 1974.

[2] K. R. Kelly, R. W. Ward, S. Treitel, and R. M. Alford, "Synthetic seismograms: A finite-difference approach," *Geophysics*, vol. 41, no. 1, pp. 2–27, 1976.

[3] K. J. Marfurt, "Accuracy of finite-difference and finite-element modeling of the scalar and elastic wave equations," *Geophysics*, vol. 49, no. 5, pp. 533–549, 1984.

[4] J. Virieux, "SH-wave propagation in heterogeneous media: Velocity-stress finite-difference method," *Geophysics*, vol. 49, no. 11, pp. 1933–1942, 1984.

[5] A. R. Levander, "Fourth-order finite-difference *P-SV* seismograms," *Geophysics*, vol. 53, no. 11, pp. 1425–1436, 1988.

[6] G. Yao, D. Wu, and H. A. Debens, "Adaptive finite difference for seismic wavefield modelling in acoustic media," *Sci. Rep.*, vol. 6, no. 1, 2016, Art. no. 30302.

[7] J.-H. Zhang and Z.-X. Yao, "Optimized finite-difference operator for broadband seismic wave modeling," *Geophysics*, vol. 78, no. 1, pp. A13–A18, 2013.

[8] E. Dormy and A. Tarantola, "Numerical simulation of elastic wave propagation using a finite volume method," *J. Geophysical Res.: Solid Earth*, vol. 100, pp. 2123–2133, 1995.

[9] M. Dumbser, M. Käser, and J. De La Puente, "Arbitrary high-order finite volume schemes for seismic wave propagation on unstructured meshes in 2D and 3D," *Geophysical J. Int.*, vol. 171, no. 2, pp. 665–694, 2007.

[10] J. D. De Basabe and M. K. Sen, "Grid dispersion and stability criteria of some common finite-element methods for acoustic and elastic wave equations," *Geophysics*, vol. 72, no. 6, pp. T81–T95, 2007.

[11] F. J. Serón, F. J. Sanz, M. Kindelan, and J. I. Badal, "Finite-element method for elastic wave propagation," *Commun. Appl. Numer. Methods*, vol. 6, no. 5, pp. 359–368, 1990.

[12] D. Komatitsch and J.-P. Vilotte, "The spectral element method: An efficient tool to simulate the seismic response of 2D and 3D geological structures," *Bull. Seismol. Soc. Amer.*, vol. 88, no. 2, pp. 368–392, 1998.

[13] E. Chaljub, D. Komatitsch, J.-P. Vilotte, Y. Capdeville, B. Valette, and G. Festa, "Spectral-element analysis in seismology," *Adv. Geophys.*, vol. 48, pp. 365–419, 2007.

[14] H. Igel, *Computational Seismology: A Practical Introduction*. Oxford, U.K.: Oxford Univ. Press, 2017.

[15] P. Moczo, J. Kristek, V. Vavryččuk, R. J. Archuleta, and L. Halada, "3D heterogeneous staggered-grid finite-difference modeling of seismic motion with volume harmonic and arithmetic averaging of elastic moduli and densities," *Bull. Seismol. Soc. Amer.*, vol. 92, no. 8, pp. 3042–3066, 2002.

[16] B. Zhang *et al.*, "An optimized choice of UCPML to truncate lattices with rotated staggered grid scheme for ground penetrating radar simulation," *IEEE Trans. Geosci. Remote Sens.*, vol. 57, no. 11, pp. 8695–8706, Nov. 2019, doi: 10.1109/TGRS.2019.2922509.

[17] W. Bao and F. L. Teixeira, "Performance analysis of perfectly matched layers applied to spherical FDTD grids," *IEEE Trans. Antennas Propag.*, vol. 66, no. 2, pp. 1035–1039, Feb. 2018, doi: 10.1109/TAP.2017.2781221.

[18] H. Chen, H. Zhou, Q. Zhang, and Y. Chen, "Modeling elastic wave propagation using K-space operator-based temporal high-order staggered-grid finite-difference method," *IEEE Trans. Geosci. Remote Sens.*, vol. 55, no. 2, pp. 801–815, Feb. 2017.

[19] Y. Zhang, J. Gao, and J. Peng, "Variable-order finite difference scheme for numerical simulation in 3-D poroelastic media," *IEEE Trans. Geosci. Remote Sens.*, vol. 56, no. 5, pp. 2991–3001, May 2018.

[20] J. L. Young, D. Gaitonde, and J. S. Shang, "Toward the construction of a fourth-order difference scheme for transient EM wave simulation: Staggered grid approach," *IEEE Trans. Antennas Propag.*, vol. 45, no. 11, pp. 1573–1580, Nov. 1997, doi: 10.1109/8.650067.

[21] L. Etemadsaeed, P. Moczo, J. Kristek, A. Ansari, and M. Kristekova, "A no-cost improved velocity-stress staggered-grid finite-difference scheme for modelling seismic wave propagation," *Geophysical J. Int.*, vol. 207, no. 1, pp. 481–511, 2016.

[22] B. Zhang, Q. Dai, X. Yin, and D. Feng, "A new approach of rotated staggered grid FD method with unsplit convolutional PML for GPR," *IEEE J. Sel. Topics Appl. Earth Observ. Remote Sens.*, vol. 9, no. 1, pp. 52–59, Jan. 2016.

[23] O. Holberg, "Computational aspects of the choice of operator and sampling interval for numerical differentiation in large-scale simulation of wave phenomena," *Geophysical Prospecting*, vol. 35, no. 6, pp. 629–655, 1987.

[24] C. Stork, "Eliminating nearly all dispersion error from FD modeling and RTM with minimal cost increase," in *Proc. 75th EAGE Conf. Exhib.*, 2013, p. cp-348.

[25] Y. Liu and M. K. Sen, "A new time–space domain high-order finite-difference method for the acoustic wave equation," *J. Comput. Phys.*, vol. 228, no. 23, pp. 8779–8806, 2009.

[26] C. Chu and P. L. Stoffa, "Determination of finite-difference weights using scaled binomial windows," *Geophysics*, vol. 77, no. 3, pp. W17–W26, 2012.

[27] H. Zhou, Y. Liu, and J. Wang, "Elastic wave modeling with high-order temporal and spatial accuracies by a selectively modified and linearly optimized staggered-grid finite-difference scheme," *IEEE Trans. Geosci. Remote Sens.*, vol. 60, 2022, Art. no. 3000122, doi: 10.1109/TGRS.2021.3078626.

[28] E. Baysal, D. D. Kosloff, and J. W. C. Sherwood, "Reverse time migration," *Geophysics*, vol. 48, no. 11, pp. 1514–1524, 1983.

[29] W.-F. Chang and G. A. McMechan, "Elastic reverse-time migration," *Geophysics*, vol. 52, no. 10, pp. 1365–1375, 1987.

[30] K. Yoon and K. J. Marfurt, "Reverse-time migration using the poynting vector," *Exploration Geophys.*, vol. 37, no. 1, pp. 102–107, 2006.

[31] W. W. Symes, "Reverse time migration with optimal checkpointing," *Geophysics*, vol. 72, no. 5, pp. SM213–SM221, 2007.

[32] X. Xiao and W. S. Leaney, "Local vertical seismic profiling (VSP) elastic reverse-time migration and migration resolution: Salt-flank imaging with transmitted *P* to *S* waves," *Geophysics*, vol. 75, no. 2, pp. S35–S49, 2010.

[33] B. Gu, Z. Li, X. Ma, and G. Liang, "Multi-component elastic reverse time migration based on the P- and S-wave separated velocity-stress equations," *J. Appl. Geophys.*, vol. 112, pp. 62–78, 2015, doi: 10.1016/j.jappgeo.2014.11.008.

[34] W. Wang and G. A. McMechan, "Vector-based elastic reverse time migration," *Geophysics*, vol. 80, no. 6, pp. S245–S258, 2015.

[35] X. Lu, A. Song, R. Qian, and L. Liu, "Anisotropic reverse-time migration of ground-penetrating radar data collected on the sand dunes in the Badain Jaran desert," *IEEE J. Sel. Topics Appl. Earth Observ. Remote Sens.*, vol. 11, no. 2, pp. 647–654, Feb. 2018, doi: 10.1109/JSTARS.2017.2787671.

[36] W. Zhang and Y. Shi, "Imaging conditions for elastic reverse time migration," *Geophysics*, vol. 84, no. 2, pp. S95–S111, 2019.

[37] H. Liu, Z. Long, F. Han, G. Fang, and Q. H. Liu, "Frequency-domain reverse-time migration of ground penetrating radar based on layered medium green's functions," *IEEE J. Sel. Topics Appl. Earth Observ. Remote Sens.*, vol. 11, no. 8, pp. 2957–2965, Aug. 2018, doi: 10.1109/JSTARS.2018.2841361.

[38] Y. Zhang *et al.*, "A 3-D high-order reverse-time migration method for high-resolution subsurface imaging with a multistation ultra-wideband radar system," *IEEE J. Sel. Topics Appl. Earth Observ. Remote Sens.*, vol. 12, no. 2, pp. 744–751, Feb. 2019, doi: 10.1109/JSTARS.2019.2892650.

[39] Q. Li, L.-Y. Fu, R.-S. Wu, and Q. Du, "A novel wavefield-reconstruction algorithm for RTM in attenuating media," *IEEE Geosci. Remote Sens. Lett.*, vol. 18, no. 4, pp. 731–735, Apr. 2021, doi: 10.1109/LGRS.2020.2982038.

[40] J. Yan and P. Sava, "Elastic wave-mode separation for VTI media," *Geophysics*, vol. 74, no. 5, pp. WB19–WB32, 2009.

[41] J. Yan and P. Sava, "Elastic wave mode separation for tilted transverse isotropy media," *Geophysical Prospecting*, vol. 60, no. 1, pp. 29–48, 2012.

[42] J. Cheng and S. Fomel, "Fast algorithms for elastic-wave-mode separation and vector decomposition using low-rank approximation for anisotropic media," *Geophysics*, vol. 79, no. 4, pp. C97–C110, 2014.

[43] G. Chen, W. Yang, Y. Liu, H. Wang, and X. Huang, "Salt structure elastic full waveform inversion based on the multiscale signed envelope," *IEEE Trans. Geosci. Remote Sens.*, vol. 60, 2022, Art. no. 4508912, doi: 10.1109/TGRS.2022.3166028.

[44] H. Kaur, S. Fomel, and N. Pham, "A fast algorithm for elastic wave-mode separation using deep learning with generative adversarial networks (GANs)," *J. Geophysical Res.: Solid Earth*, vol. 126, no. 9, 2021, Art. no. e2020JB021123.

[45] Y. Wei *et al.*, "Deep learning-based P- and S-wave separation for multi-component vertical seismic profiling," *IEEE Trans. Geosci. Remote Sens.*, vol. 60, 2022, Art. no. 5908116, doi: 10.1109/TGRS.2021.3124413.

[46] M. Kindelan, M. Moscoso, and P. Gonzalez-Rodriguez, "Optimized finite difference formulas for accurate high frequency components," *Math. Problems Eng.*, vol. 2016, 2016, Art. no. 7860618.

[47] W. Liang, X. Wu, Y. Wang, and C. Yang, "A simplified staggered-grid finite-difference scheme and its linear solution for the first-order acoustic wave-equation modeling," *J. Comput. Phys.*, vol. 374, pp. 863–872, 2018.

[48] Y. Wang, W. Liang, Z. Nashed, X. Li, G. Liang, and C. Yang, "Seismic modeling by optimizing regularized staggered-grid finite-difference operators using a time-space-domain dispersion-relationship-preserving method," *Geophysics*, vol. 79, no. 5, pp. T277–T285, 2014.

[49] Y. Liu and M. K. Sen, "Scalar wave equation modeling with time-space domain dispersion-relation-based staggered-grid finite-difference schemes," *Bull. Seismol. Soc. Amer.*, vol. 101, no. 1, pp. 141–159, 2011.

Wenquan Liang was born in Henan Province, China. He received the Ph.D. degree in geophysics from the Institute of Geology and Geophysics, Chinese Academy of Sciences, Beijing, China, in 2012.

Since 2014, he has been a Vice Professor with Longyan University, Fujian, China. His research interests include FDTD wave equation modeling, optimization methods, and reverse-time migration.

Guoxin Chen received the B.S. degree in mathematics from Shandong University, Jinan, China, in 2011, and the Ph.D. degree in geophysics from Zhejiang University, Zhoushan, China, in 2018.

He was a Visiting Scholar with the University of California, Santa Cruz, CA, USA, from 2014 to 2019. He is currently an Associate Researcher with Zhejiang University, Zhoushan, China. His research interests include seismic full waveform inversion, prestack depth migration, seismic wave simulation, and geophysical signal processing.

Yanfei Wang received the B.S. degree in mathematics from Hebei Normal University in 1997, and the Ph.D. degree in computational mathematics from Academy of Mathematics and System Science, Chinese Academy of Sciences, in 2002.

He is currently a Professor with the Institute of Geology and Geophysics, Head of the Center of Big Data Analysis and Intelligent Computing, Director of the Key Laboratory of Petroleum Resources Research, Chinese Academy of Sciences, Beijing, China.

His research interests include computational and exploration geophysics, big data and artificial intelligence analysis in earth sciences.

Jingjie Cao received the Ph.D. degree in solid geophysics from Graduate School of Chinese Academy of Sciences, in 2011.

He is currently a Professor of Hebei GEO University. He once worked as a Postdoctoral Researcher with the University of California, Santa Cruz, CA, USA, for one year.

His research interests include seismic exploration signal processing, geophysical inversion theory, optimization method and application of artificial intelligence in geophysical signal processing.

Jinxin Chen received the B.E. degree in software engineering from the Zhongyuan University of Technology, Zhengzhou, China, in 2020. He is currently working toward the M.E. degree in geophysics with Zhejiang University, Zhoushan, China, under the supervision of Associate Researcher Guoxin Chen.

His research interests include seismic data denoising and data processing.